Article

Macroscopic and Microscopic Levels of Methylene Blue Adsorption on a Magnetic Bio-Based Adsorbent: In-Depth Study Using Experiments, Advanced Modeling, and Statistical Thermodynamic Analysis

Mohamed A. Ali [1,*], Aliaa M. Badawy [2], Ali Q. Seliem [2], Hazem I. Bendary [3], Eder C. Lima [4,5], M. Al-Dossari [6], N. S. Abd EL-Gawaad [7], Glaydson S. dos Reis [8,9], Mohamed Mobarak [10], Ali M. Hassan [11] and Moaaz K. Seliem [2]

[1] School of Biotechnology, Badr University in Cairo (BUC), Badr City 11829, Egypt
[2] Faculty of Earth Science, Beni-Suef University, New Bani Suef City 62511, Egypt; mohamedaliaa729@yahoo.com (A.M.B.); aliselimq@gmail.com (A.Q.S.); debakyms@yahoo.com (M.K.S.)
[3] Chemical Engineering Department, Higher Institute of Engineering, El-Shorouk Academy, Shorouk City 11837, Egypt; hazemibrahem31@yahoo.com
[4] Postgraduate Program in Mine, Metallurgical, and Materials Engineering (PPGE3M), School of Engineering, Federal University of Rio Grande do Sul (UFRGS), Av. Bento Gonçalves 9500, Porto Alegre 91501-970, RS, Brazil; eder.lima@ufrgs.br
[5] Institute of Chemistry, Federal University of Rio Grande do Sul (UFRGS), Av. Bento Goncalves 9500, P.O. Box 15003, Porto Alegre 91501-970, RS, Brazil
[6] Dhran Aljanoub, Applied College, King Khalid University, Abha 62529, Saudi Arabia; mdosri@kk.edu.sa
[7] Muhayil Asir, Applied College, King Khalid University, Abha 62529, Saudi Arabia; nshat@kku.edu.sa
[8] Laboratory of Industrial Chemistry and Reaction Engineering, Faculty of Science and Engineering, Åbo Akademi University, 20500 Åbo/Turku, Finland; glaydsonambiental@gmail.com
[9] Department of Forest Biomaterials and Technology, Biomass Technology Centre, Swedish University of Agricultural Sciences, SE-901 83 Umeå, Sweden
[10] Physics Department, Faculty of Science, Beni-Suef University, New Bani Suef City 62511, Egypt; saidan2011@yahoo.com
[11] Physics and Engineering Mathematics Department, Higher Institute of Engineering, El-Shorouk Academy, Shorouk City 11837, Egypt; eldeeb1983dedo@gmail.com
* Correspondence: mohamed.ahmed_ali@buc.edu.eg

Abstract: A magnetic bio-based adsorbent derived from H_2O_2-activated zeolite and turmeric carbohydrate polymer was fabricated, characterized, and utilized in removing methylene blue (MB) dye at pH 8.0 and temperatures between 25 and 55 °C. To understand the molecular-scale adsorption mechanism, a range of advanced statistical physics models were employed in conjunction with conventional equilibrium models. The as-synthesized biosorbent presented high maximum capacities according to the Langmuir model, with values ranging from 268.67 to 307.73 mg/g. The double-layer equation yielded the best-fitting results to the MB experimental data among the applied statistical physics models. The number of MB molecules ranged from 1.14 to 1.97, suggesting a multi-molecular mechanism with a non-parallel orientation. The main factor affecting the effectiveness of this adsorbent was the density of its functional groups, which varied from 27.7 to 142.1 mg/g. Adsorption energies in the range of 19.22–21.69 kJ/mol were obtained, representing the existence of physical forces like hydrogen bonds and electrostatic interactions. To complete the macroscopic examination of the MB adsorption mechanism, thermodynamic parameters such as entropy, Gibbs free energy, and internal energy were considered. The adsorption/desorption outcomes up to five cycles displayed the stability of the magnetic biosorbent and its potential for decontaminating industrial effluents. Overall, this work increases our understanding of the MB adsorption mechanism onto the produced biosorbent at the molecular level.

Keywords: activated zeolite; iron oxide; turmeric polymer; methylene blue; adsorption; advanced modeling; reusability

1. Introduction

The significant industrial revolution of the last few decades has contributed to an increase in the contamination of water bodies with different stable chemical compounds, including organic dyes [1–5]. In the long run, dye pollution may have teratogenic and carcinogenic effects, posing a serious threat to both human health and the ecosystem [6–8]. Methylene blue (MB), a synthetic dye used in the paper, plastic, and textile industries, is very difficult to eliminate from wastewater because of its complex molecular structure and resistance to biodegradation [9]. Consequently, the development of highly effective, commercially feasible, and environmentally safe technologies for the treatment of dye-contaminated wastewater is urgently required. Both inorganic and organic chemicals have been removed from water using a variety of techniques, including, adsorption, membrane filtration, precipitation, coagulation, biological treatment, and advanced oxidation [10–14]. Because of its ease of use, great efficacy, and availability, adsorption is frequently selected among these techniques for water remediation [7,15–20]. Overall, recent studies have concentrated on generating novel magnetic biocomposites that are non-toxic, readily synthesized, easily separated, and biodegradable to remove contaminants from water with high efficiency [21].

Natural zeolite (NZ) is a type of hydrated aluminosilicate that features a framework structure composed of micropores, channels, and cavities. Due to their unique 3D porous structure, negatively charged surface, and their cation-exchange capacity, zeolites are effective in removing different pollutants, such as heavy metals and basic dyes [22–24]. The minerals of NZ are divided into a number of groups, and each collection exhibits a unique adsorption behavior and performance in the field of water remediation [23]. Natural and synthetic zeolites have several advantages over other materials for the removal of water pollutants due to the following characteristics: low cost, high reserves, excellent surface area, high safety, and remarkable chemical stability [25]. Furthermore, zeolite-based composites (e.g., Fe_3O_4/zeolite, Fe_3O_4/activated zeolite, and chitosan/zeolite) were made and applied as effective adsorbents to eliminate a variety of pollutants from wastewater [25–27].

Turmeric, also known as *Curcuma longa* L., is a well-known ancient spice with a long history of use because of its flavor and therapeutic qualities. Based on economic and environmental assessments, this naturally occurring carbohydrate is inexpensive and widely accessible [13,14]. Turmeric-based adsorbents have attracted a lot of interest and have been effectively used to remove phenol and MB dye from aqueous solutions [28].

Magnetic nanoparticles (MNPs) are characterized by distinctive characteristics, including large surface areas, available active sites, bio-compatibility, and ease of extraction from aqueous solutions through the application of an external magnetic field [29–31]. However, in solutions, iron oxide nanoparticles tend to group together, which reduces their capacity to eliminate contaminants from water [29,30]. As a result, raw and/or treated materials supported by MNPs can be designed and used as effective and environmentally friendly adsorbents for water pollution [31–33].

When MNPs are combined with aluminosilicates and natural carbohydrate polymers, a class of clean composites is produced that have significant surface areas, high efficiency, and a lot of multifunctional chemical adsorption sites. Thus, the novel contribution of this work was to generate a biodegradable and eco-friendly magnetic nanocomposite by loading the combination between activated natural zeolite and turmeric polymer with magnetite nanoparticles. The performance of the produced ANZ/TC/MNPs as a workable and cost-effective adsorbent for extracting MB from solutions was considered. Alternative techniques (e.g., XRD, FESEM, DSC, TGA, FTIR, TEM, BET surface area, and zeta potential) were used to characterize the produced ANZ/TC/MNPs composite. The energetic and steric parameters derived from the statistical physics models were applied in addition to conventional isotherm models to clarify the adsorption mechanism. Understanding the interface mechanism between the MB molecules and the ANZ/TC/MNPs composite at both the macroscopic and microscopic scales can be reliably achieved by utilizing the statistical physics theory.

2. Materials and Methods

2.1. Materials

The turmeric (TC) sample used in this study was locally sourced from a company in Egypt. The natural zeolite (NZ) was supplied from a zeolite mine in Taiz city, Yemen. Both NZ and TC samples were ground to achieve particle sizes below 100 μm. Iron chloride ($FeCl_2$), hydrogen peroxide (H_2O_2, 30%), and NH_4OH solution were supplied by Loba Chemie in India and used in this work. In this investigation, the tested methylene dye (MB) was purchased from Sigma-Aldrich. Diluted solutions of NaOH and HCl were used to regulate the starting pH values before carrying out the uptake experiments.

2.2. Synthesis of ANZ/TC/MNPs Composite

In the first step, Fe_3O_4 nanoparticles (MNPs) were formed using activated altered basalt via the precipitation process outlined in [34]. In a beaker with 30 mL deionized water, 0.75 g of $FeCl_2$ and 1.5 g of heated altered basalt powder were combined. Then, 10 mL of NH_4OH was added and the mixture was stirred until the precipitation of MNPs with a black color. In a separate step, 15 mL of H_2O_2 was added to a second beaker that contained 25 mL of distilled water and 2.0 g of NZ with continuous stirring for 2 h at 40 °C. The H_2O_2/NZ mixture (ANZ) was then combined with 1.0 g of cleaned and dried TC with stirring for 3 h. The MNPs from the first stage and the ANZ/TC of the second step were then mixed for 3 h at 25 °C. Using an external magnet, the induced magnetic ANZ/TC/MNPs adsorbent was separated. It was then repeatedly cleaned with distilled water and baked for 24 h at 70 °C in an oven. After being created, the fabricated composite was carefully ground in agate mortar and kept for analyzing and MB adsorption examinations. Figure 1 shows the processes needed to prepare the ANZ/TC/MNPs adsorbent.
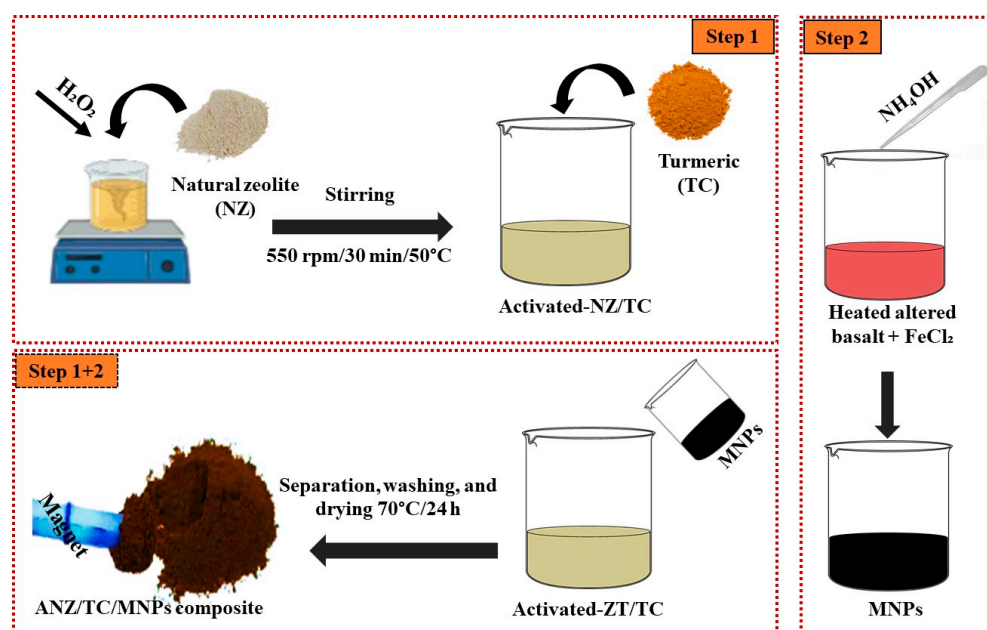
Figure 1. The procedures used to prepare the tested ANZ/TC/MNPs adsorbent.

2.3. Characterization of ANZ/TC/MNPs

A Philips APD–3720 diffractometer operating with Cu Kα radiation at 40 kV and 40 mA was used to analyze the XRD pattern of ANZ/TC/MNPs. At a scanning speed of 10° per min, the diffraction patterns covered a diffractive angle range of 5° to 65°. Field-emission scanning electron microscopy (FESEM, Sigma 500 VP, Zeiss, Oberkochen, Germany) was used to examine the composite's structural characteristics. The functional groups embedded in the created composite were ascertained by Fourier-transform infrared (FTIR-2000) spectroscopy, PerkinElmer, Waltham, MA, USA, which was used with a scan-

ning wavenumber between 4000 and 400 cm^{-1}. Transmission electron microscopy (TEM), Thermo Fisher Scientific, Waltham, MA, USA, was used to examine the internal microstructure and particle morphology of the used adsorbent. The magnetic measurements were carried out using a vibrating sample magnetometer (VSM), Lake Shore Cryotronics, Westerville, OH, USA. Differential scanning calorimetry (DSC) and thermogravimetric (TGA), PerkinElmer, Waltham, MA, USA, analyses of ANZ/TC/MNPs were carried out in the 25–1000 °C range using a Labsys evo equipment under a heating rate of 10 °C/min. The ZN/TC/MNPs' zeta potential was determined using the Nano ZS90 Zetasizer, Malvern Panalytical, Worcestershire, UK. We used the following procedure to determine the zeta potential of the prepared ANZ/TC/MNPs: Using an ultrasonic bath for 30 min, 0.01 g of ANZ/TC/MNPs was added to 250 mL of distilled water before measurement. Then, at 25 °C, an electrical field of 150 mV was applied to a folded capillary cell containing 1 mL of the suspension. The Brunauer–Emmett–Teller (BET), HORIBA Scientific, Kyoto, Japan, approach was used to measure the BET surface area (S$_{\text{BET}}$) of the as-synthesized adsorbent [35].

2.4. MB Adsorption Isotherm Studies on ANZ/TC/MNPs Composite

The adsorption isotherms of MB, with changing the initial solution concentration (C_0, 25–200 mg/L), were confirmed at a solution pH value of 8.0 and temperatures of 25, 40, and 55 °C.

An RS9000 shaker was used to mix all combinations of ANZ/TC/MNPs (50 mg) and MB solution (50 mL) at 150 rpm for 120 min to attain the equilibrium stage. All adsorption experiments were completed three times, and the average values of the results, with an error range that was always of less than ±5%, were used to evaluate the data. An external magnet was used to separate the ANZ/TC/MNPs composite from the liquid phases. An ultraviolet–visible spectrophotometer was used to measure the residual MB dye concentrations at λ_{max} = 660 nm. The developed adsorbent removed MB molecules at equilibrium (q_e, mg/g) in the amounts calculated via the next relation.

$$q_e(\text{mg/g}) = (C_0 - C_e)\frac{V}{m} \tag{1}$$

where V the volume (L) of the MB solution and m is the mass (g) of NZ/TC/MNPs.

2.5. Conventional Modeling for MB-ANZ/TC/MNPs Interaction

For modeling the MB data, the non-linear techniques of the most widely used conventional Langmuir [36] and Freundlich [37] equations were selected. Further details regarding the mathematical expressions for these classical equations can be found in the Supplementary Materials.

2.6. Statistical Modeling for ANZ/TC/MNPs Interaction

Three unconventional (i.e., multilayer, double-layer, and monolayer) statistical physics models were also used to explain the removal of MB molecules by the ANZ/TC/MNPs adsorbent. In addition to the results of conventional models, the complicated physics models offered more understanding of the behavior of the MB-ANZ/TC/MNPs adsorption system. More information about the references and mathematical formulations of these adsorption equations is provided in the Supplementary Materials [9,21,34].

2.7. Thermodynamic Functions of MB Adsorption

Analyzing thermodynamic functions from the perspective of statistical physics theory helps in understanding the interface between the ANZ/TC/MNPs and the MB molecules. Thermodynamic functions, which are detailed in the Supplementary Materials, were interpreted using the best-adjusted adsorption model [21].

2.8. Effect of NaCl Concentration on Dye Adsorption

Due to the dyeing process usually being associated with a rise in salt concentration, MB adsorption onto the MNPS-G/CA was examined in relation to the amount of sodium chloride in solution. The influence of salt content on MB was investigated using 50 mL of the dye under study at a concentration of 100 mg/L and a mass of 50 mg of ANZ/TC/MNPs. Various NaCl concentrations extending between 0.2 and 1.2 g/L were employed to check the salinity impact.

2.9. Regeneration of ANZ/TC/MNPs Adsorbent

The tested adsorbent's financial feasibility was assessed using a recycling method. Using ethanol as a desorbing agent, experiments on the regeneration and reuse of the formed composite were carried out at 25 °C. ANZ/TC/MNPs (0.5 g) containing 100 mL of MB molecules were shaken at 150 rpm for a duration of 2 h. In this study, five rounds of MB adsorption/desorption were employed. The ANZ/TC/MNPs was used in the next round after being cleaned with distilled water and dried at 70 °C for 16 h after each cycle.

3. Result and Discussions

### 3.1. Characterization of ANZ/TC/MNPs Adsorbent

Using the X-ray diffraction (XRD) technique, the phases of the studied ANZ/TC/MNPs adsorbent were identified as displayed in Figure 2. The resulting pattern exhibited the characteristic peaks of natural zeolite, which were observed at 2θ angles of approximately 9.88°, 11.2°, 19.1°, 24°, 26.88°, and 28.15° [25]. Moreover, additional new peaks located at 2θ = 35.76°, 43.62°, 57.25°, and 63.05 were detected, as shown in Figure 2. These peaks that formed correspond to the (311), (400), (511), and (440) lattice planes of the as-prepared MNPs [11]. The card numbers utilized to identify the natural zeolite and the synthesized Fe_3O_4 phases were 25-1349 and 00-075-0449, respectively. Accordingly, the XRD result is in agreement with the Fe_3O_4 nanoparticles (MNPs) being incorporated into the NZ/TC biocomposite producing the investigated ANZ/TC/MNPs nanocomposite.
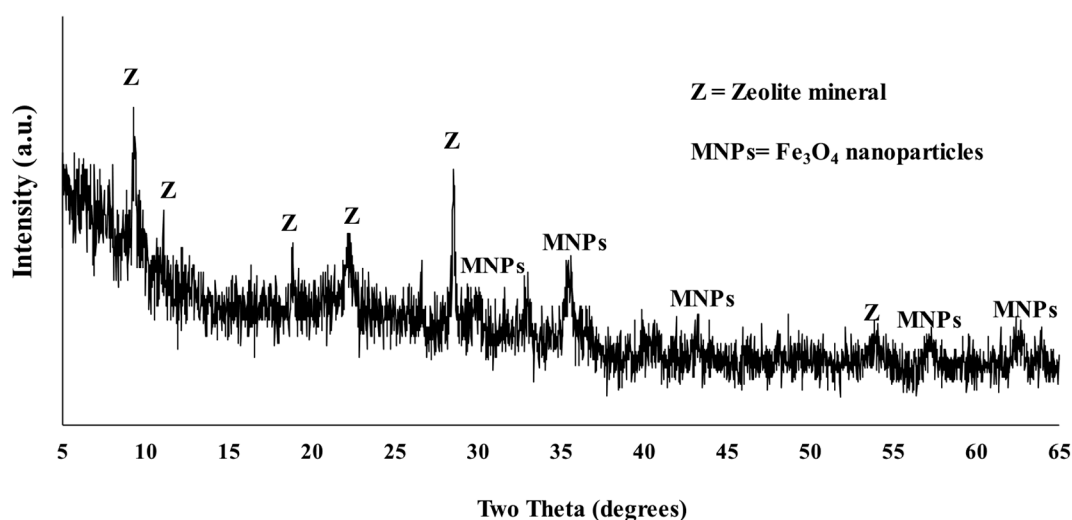
Figure 2. XRD outline of the prepared ANZ/TC/MNPs adsorbent.

The FTIR spectrum of ANZ/TC/MNPs shows a variety of absorption bands (Figure 3). The bands observed at 3413.73 and 1639.36 cm^{-1} are associated with water molecules, which represent the existence of physically adsorbed water within the studied sample [38]. The asymmetric stretching of Si–O or Al–O is associated with the vibration at 1037.92 cm^{-1}, whereas the Fe–O functional group of Fe-bearing minerals is linked to the bands found at 467.06 and 599.36 cm^{-1} [34]. The bands observed at 791.07 cm^{-1} and 1326.26 cm^{-1} are

related to Al–O–Al and water of NZ, respectively [11,26]. Additionally, the detected peaks at 2851.56 and 2928.56 cm^{-1} are related to the C–H bonds stretching [39].
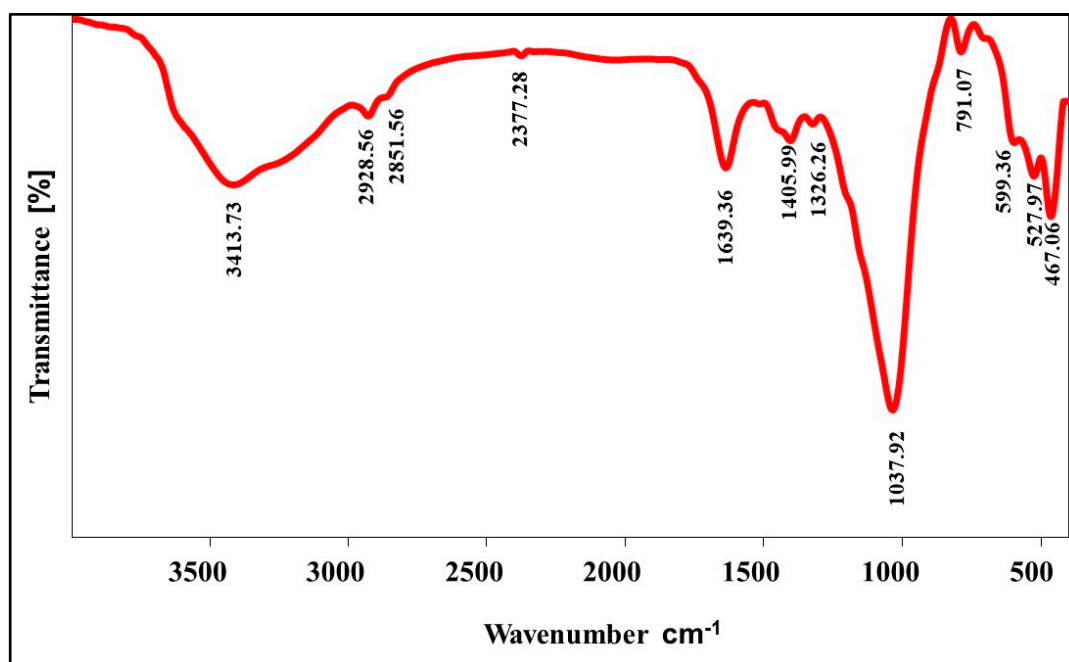

Figure 3. FTIR spectrum of the prepared ANZ/TC/MNPs composite.

Characteristic FESEM and TEM images of the considered ANZ/TC/MNPs composite are illustrated in Figure 4. The irregular particles that appear as micro-aggregates with a flaky morphology are typical for NZ. The interaction between the H$_2$O$_2$ solution and the NZ grains caused the zeolite's structural bonds to break, increasing its porosity (ANZ). Additionally, changing the thickness of the NZ sheets may also related to the peroxide activation. The carbohydrate TC that is used has particles of different sizes and shapes, including irregular and rod-like forms. By entering TC particles inside the formed NZ's pores and holes, the ANZ/TC interface was generated. On the ANZ and ANZ/TC surfaces, Fe$_3$O$_4$ aggregates or scatters in the form of spherical-like particles with a diameter of less than 25 nm. Moreover, a collection of numerous faceted Fe$_3$O$_4$ particles can be seen, as shown in Figure 4a–d. Additionally, the dispersed NZ sheets have the ability to partially prevent the accumulation of iron oxide nanoparticles. Avoiding the MNPs' aggregation in solution is very helpful in enhancing the MB–adsorbent interaction. In general, these magnetic nanoparticles can help in developing adsorbents with promising potentials for the removal of various water contaminants [12].

The TEM images (Figure 4e,f) show a large number of irregularly shaped light and dark areas. The TEM image's bright spots indicated the existence of the ANZ/TC interface in the absence of MNP support. Upon decorating ANZ/TC with Fe$_3$O$_4$, a mass of nearly uniform, dark spherical objects is observed, in agreement with the anticipated morphology of iron oxide nanoparticles. Fe$_3$O$_4$ nanoparticles are clearly visible, despite some grouping that is typical given their magnetic properties. As a result, the FESEM and TEM results proved that ANZ/TC was successfully coated with Fe$_3$O$_4$ nanoparticles.

In order to determine the particle size of the tested adsorbent, 50 particles were measured using ImageJ software (release/version 2.15.1), and the histogram of the particle size distribution is displayed in Figure 4g. Based on the attained histogram of ANZ/TC/MNPs, the greatest number of particles was concentrated in the 9–10 nm range. Statistical data revealed that the magnetic ANZ/TC/MNPs biosorbent had a particle size with an average of 9.27 nm. Furthermore, the standard deviation in the particle size distribution of ANZ/TC/MNPs adsorbent was equal to 1.98 nm, which indicated a slighter size distribu-

tion for the studied adsorbent. The distinct particle size distribution for ANZ/TC/MNPs confirmed the high performance of the developed adsorbent in removing MB dye from solutions [40,41]. The magnetic behavior of the examined magnetic-bio-based adsorbent (ANZ/TC/MNPs) was investigated at room temperature using a vibrating sample magnetometer. The magnetic hysteresis loop of this magnetic adsorbent is displayed in Figure 4h. The saturation magnetization was found to be 26.62 emu/g.
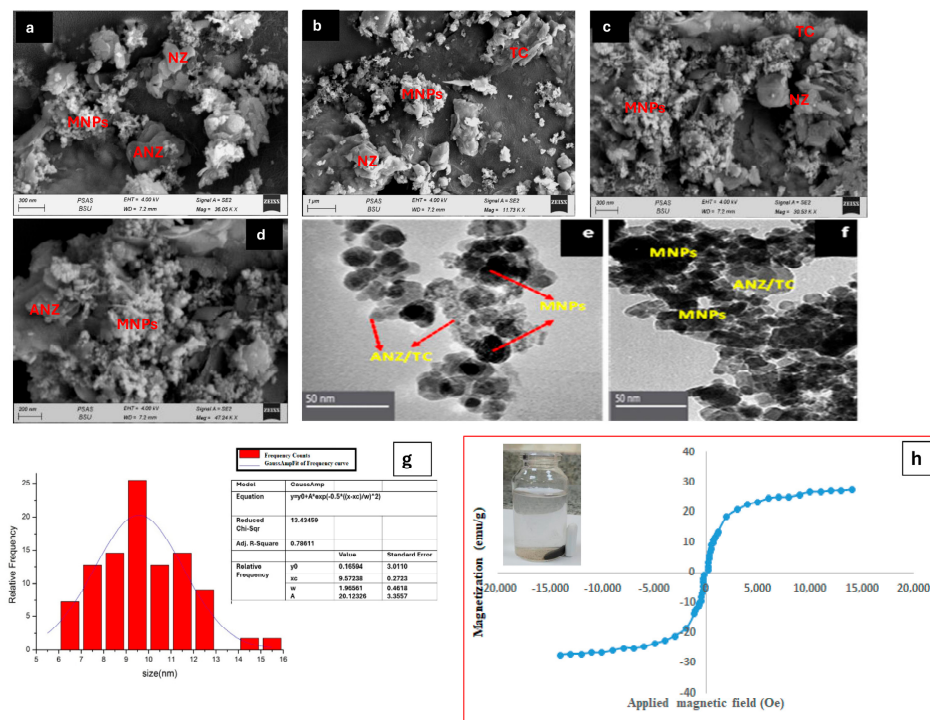
Figure 4. FESEM (**a**–**d**), TEM (**e**,**f**) images, particle size distribution histogram (**g**) and magnetic hysteresis curve of ANZ/TC/MNPs composite (**h**).

For the studied ANZ/TC/MNPs adsorbent, the TGA curve shows two notable weight loss events that happen at different temperature ranges (Figure 5). The TGA analysis indicates an initial minor weight loss (1.72% at a temperature below 200 °C, which is likely attributed to the evaporation of mechanically bound water and elimination of other impurities [42]. In the second phase, a weight loss (~7.86%) is observed within the temperature range of 200–600 °C, which could be related to the oxidation of organic components and the degradation of the hydroxyl (-OH) groups in the ANZ/TC/MNPs structure [43]. The last stage of weight loss (600–800 °C) is assigned to the release of oxygen during the oxidation of Fe_3O_4 to form the hematite phase and the complete decomposition of the developed ANZ/TC/MNPs adsorbent [21,42]. Furthermore, the DSC curve reveals three prominent peaks. The first peak, which is observed between 100 and 150 °C, is likely related to the evaporation of H_2O molecules. The release of organic matter and chemically held water from the ANZ/TC/MNPs composite may be the reason of the second peak, which occurred between 200 and 600 °C. The final peak, around 600–800 °C, is associated with the comprehensive dehydroxylation of zeolite and the formation of hematite (Fe_2O_3) mineral [42]. Overall, the TGA and DSC findings demonstrate the high stability of ANZ/TC/MNPs adsorbent until 600 °C.
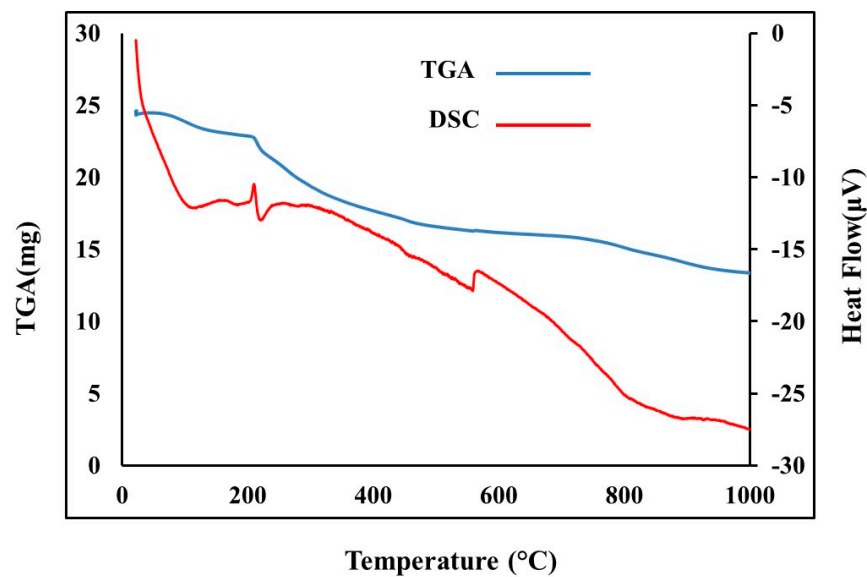
Figure 5. DSC and TGA curves of ANZ/TC/MNPs composite.

The nitrogen adsorption–desorption measurements of ANZ/TC/MNPs and BJH pore sizing distributions are presented in Figure 5. Based on the International Union of Pure and Applied Chemistry (IUPAC) category [44], the ANZ/TC/MNPs exhibits a type IV isotherm plot featuring an H_3 hysteresis curve observed in the 0.3–1 range. This hysteresis loop represents the mesopore structure of the developed ANZ/TC/MNPs composite with the existence of slit-like pores and cylindrical pores [45]. The specific surface area and the average pore diameter of ANZ/TC/MNPs were 13.148 m^2/g and 21.859 nm, respectively (see Figure 6). The pore size distribution function obtained by BJH-model (Figure 6b) was found to be around 13.647 nm. This distribution can improve the pores' accessibility, which makes it easier for MB molecules to diffuse and interact throughout the adsorption processes.
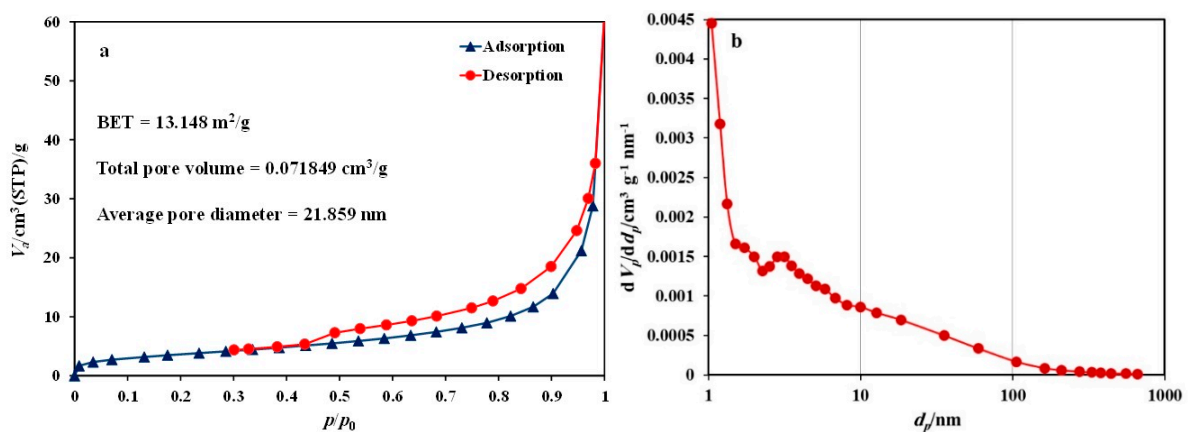

Figure 6. BET surface area (**a**) and pore size distribution (**b**) of ANZ/TC/MNPs composite.

3.2. pH Effect and Zeta Potential Calculation

The effect of changing the pH of the solution from 2.0 to 10.0 on the ANZ/TC/MNPs adsorbent's ability to remove MB dye is shown in Figure 7a. The ANZ/TC/MNPs surface becomes protonated when exposed to high concentrations of H$^+$ ions at pH 2.0 and 4.0, which are extremely acidic conditions. As a result, the uptake percentages are reduced to 21% (pH 2.0), 29% (pH 3.0), and 39% (pH 4.0) due to the strong repulsive forces between the protonated functional groups of the adsorbent and the positive MB molecules. On the other hand, MB removal percentages increased from 63% to 87% when the pH was raised

from 6.0 to 7.0. The active sites of the ANZ/TC/MNPs adsorbent most likely deprotonated, improving the removal of MB. Finally, the electrostatic attraction between the negatively charged sites of the ANZ/TC/MNPs and the MB ions produced the optimum values of MB uptake at pH 8.0 and 10.0.
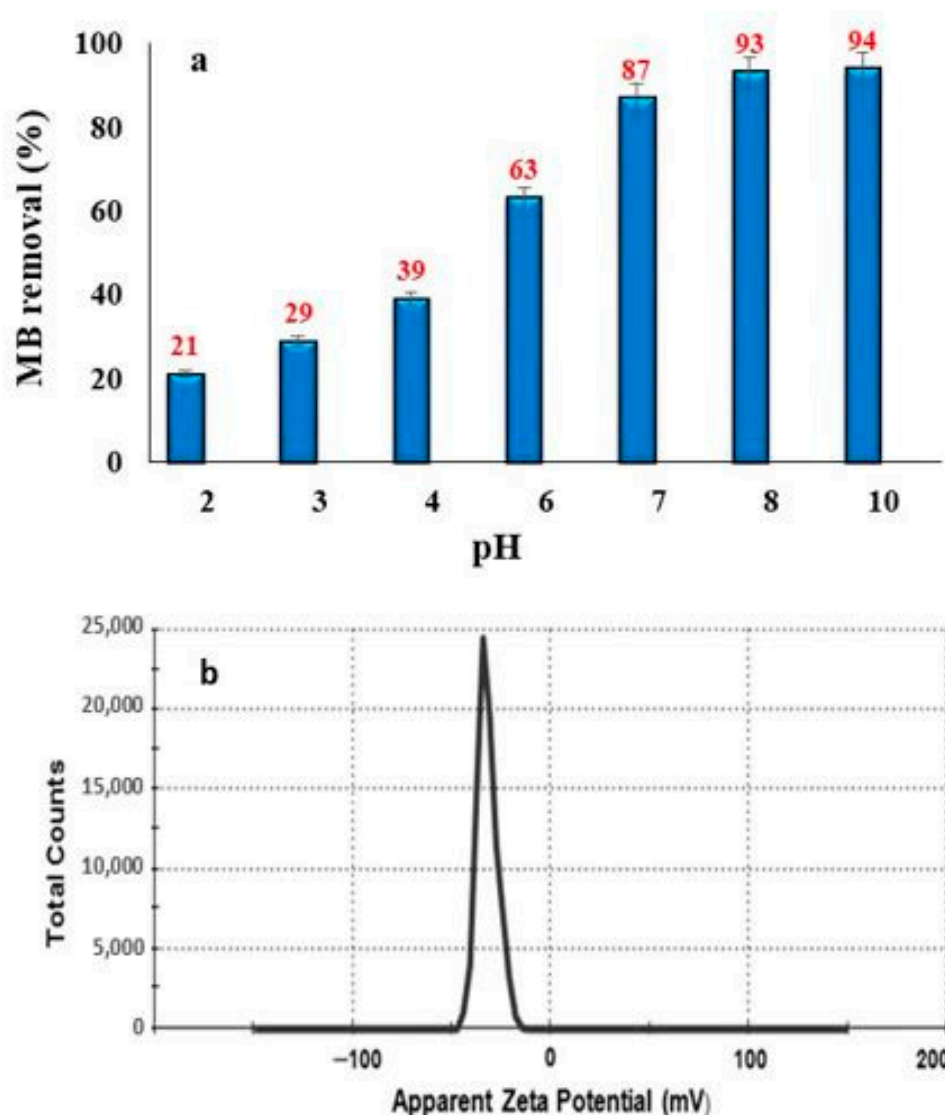
Figure 7. MB removal as a function of pH (**a**) and zeta potential (**b**) of ANZ/TC/MNPs composite.

According to Horie and Fujita [46], nanoparticles with zeta potentials (ZP) $\geq +25$ mV or < -25 mV are generally considered to be highly stable. A negative zeta potential of -28.3 mV was observed in the ANZ/TC/MNPs composite (Figure 7b). The ZP value decreased with increasing solution pH, which was explained by an increment in the number of hydroxyl ions in the solution as well as the deprotonation of the functional groups in the adsorbent. The ANZ/TC/MNPs' surface bears a significant negative charge, which supported its strong stability against aggregation [46]. Therefore, a pH of 8.0 was chosen for the solution in all of the MB adsorption experiments based on the pH experiment and zeta potential quantities.

3.3. Classical Modeling

The parameters derived from classical fitting of the MB adsorption data to the non-linear forms (Figure 8) are listed in Table 1. The R^2 values indicated that MB adsorption on the ANZ/TC/MNPs adsorbent was described by these models at temperatures of 25, 40,

and 55 °C ($R^2 > 0.98$). Therefore, the best classical model was selected using the Chi-square values. The affinity of the Freundlich model to fit the experimental data was confirmed by the lowest χ^2 value across all temperatures, as seen in Table 1. Consequently, different functional groups of ANZ/TC/MNPs led to the foundation of several MB layers. The monolayer capacities (q_{max}) were 268.67, 290.28, and 307.73 mg/g at 25, 40, and 55 °C, respectively (see Table 1). The rise in (q_{max}) as the temperature increased indicated that the interface of MB–ANZ/TC/MNPs was driven by an endothermic type. Notably, when the solution temperature rose from 25 to 55 °C, the K_F increased from 5.97 to 12.51 mg/g, verifying the endothermic reaction between MB and the ANZ/TC/MNPs adsorbent. Additionally, the $1/n_F$ values (Table 1) ranged from 0.735 to 0.720 (i.e., all values were <1.0), implying a favorable removal process at small concentrations of MB dye [47,48].
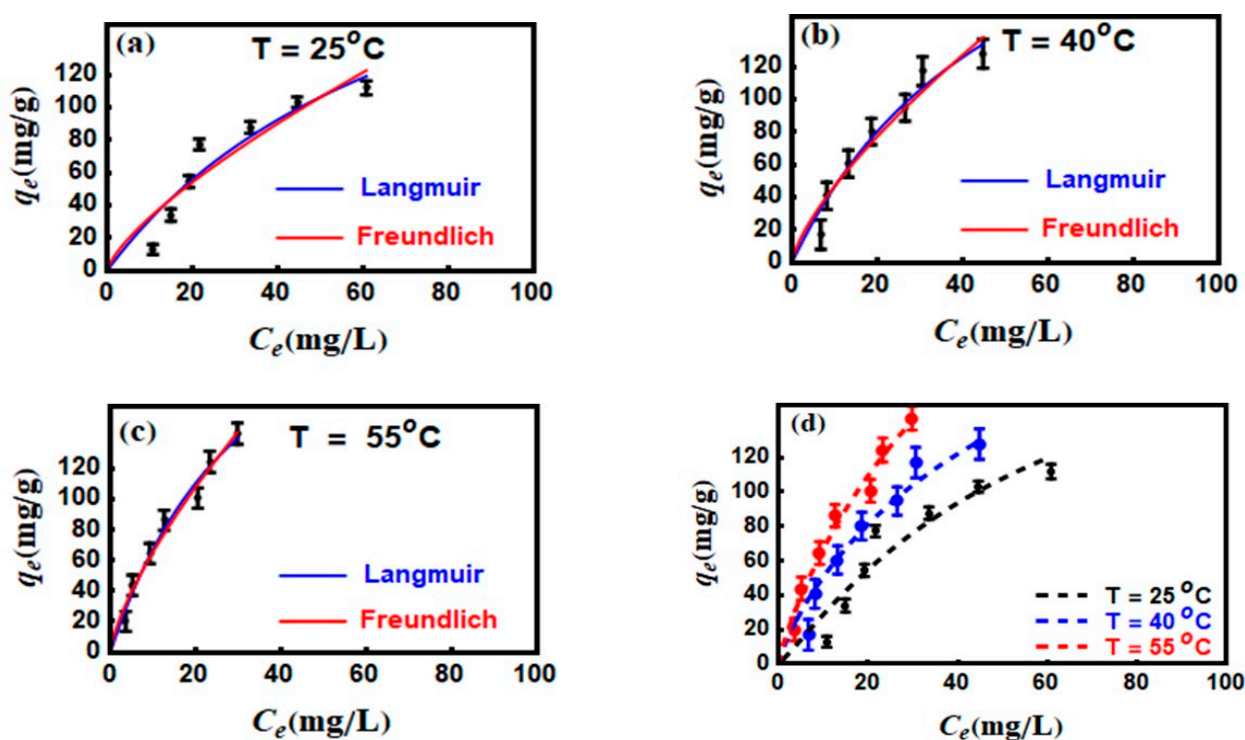

Figure 8. MB adsorption modeling using the classical (**a**–**c**), and the double-layer models (**d**).

Table 1. Parameters of the conventional models used in fitting MB adsorption data.

Isotherm Model		Parameters			
Langmuir	**T (°C)**	$q_{\mathbf{max}}$**(mg/g)**	K_L**(L/mg)**	R^2	χ^2
	25	268.67	0.018	0.9772	6.31
	40	290.28	0.019	0.9817	5.42
	55	307.73	0.028	0.9854	4.31
Freundlich		K_F $\left((\text{mg/g})(\text{mg/L})^{-1/n}\right)$	$1/nF$		
	25	5.97	0.735	0.9914	5.81
	40	8.91	0.721	0.9974	4.72
	55	12.51	0.720	0.9986	3.64

3.4. Statistical Physics Modeling

Since statistical advanced models involve a number of steric and energetic components, their application is generally crucial to comprehending the adsorption behavior. The position of dye molecules and the molecular-scale interaction mechanism can be clearly seen by interpreting these physicochemical parameters at each temperature. It is crucial

to clarify that these details cannot be provided by the parameters that arrived from the classical models. The results of the R^2 and RMSE calculations for the values given in Table S1 showed that the double-layer model with two adsorption energies (Model 2) fitted the MB adsorption data well (i.e., $R^2 > 0.99$ and RMSE ranged from 0.78 to 1.35). Thus, using the double-layer model, the *n*, N_M, and Q_{sat} (steric) and ΔE (energetic) parameters were computed and analyzed. As previously indicated, the Supplementary Materials present the assumptions for these models as well as the identification of the related parameters [21,34].

3.5. Insights into the MB Uptake Mechanism via Steric Parameters E Interpretation
3.5.1. The n Parameter

According to Badawy et al. [21], the MB adsorption mechanism can be described by three conditions, all of which are characteristically supplied by the number of molecules per active site (i.e., the *n* parameter).

First condition (*n* < 0.5): two or more ANZ/TC/MNPs active sites may share an adsorbed MB molecule, offering a horizontal orientation and multi-docking mechanism.

Second condition (0.5 < *n* < 1): asymmetric geometries, such as vertical and horizontal adsorption positions, distinguish the MB-ANZ/TC/MNPs interfaces.

Third condition (*n* ≥ 1): one or more MB molecules can be removed by the ANZ/TC/MNPs functional groups, suggesting a vertical orientation and multi-molecular mechanism.

Figure 9 shows the solution temperature performance of the steric *n* parameter, which is associated with MB adsorption onto ANZ/TC/MNPs.
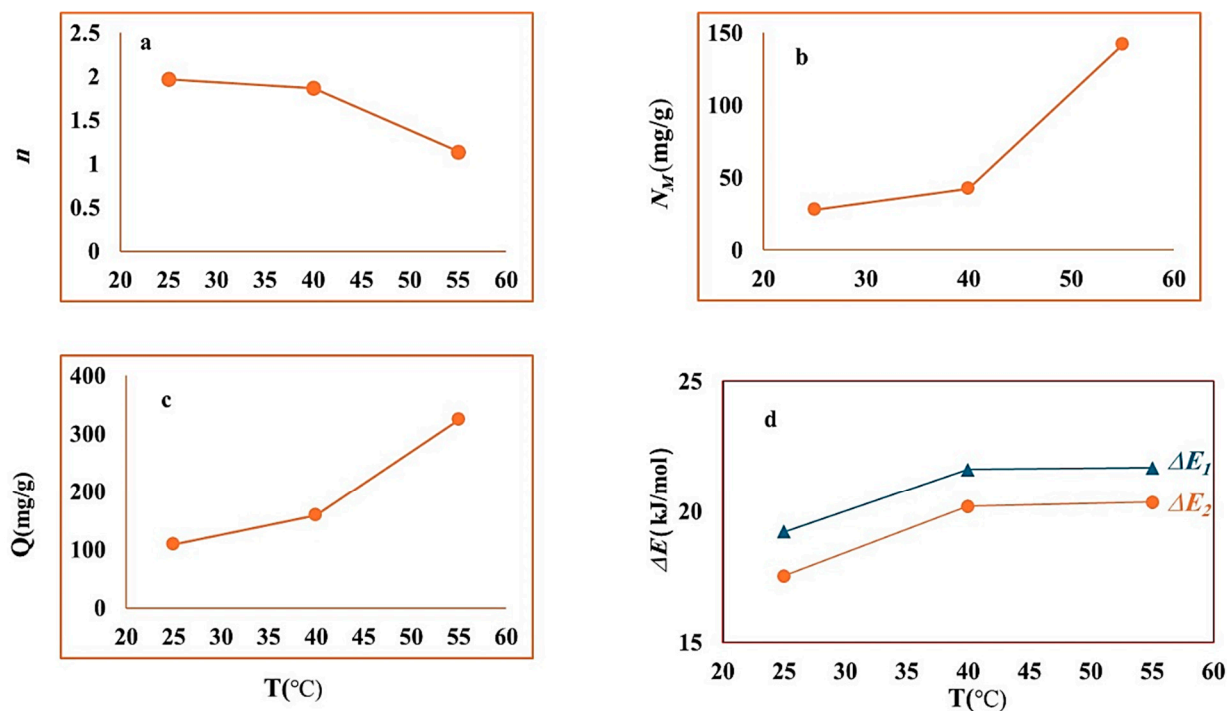
Figure 9. Calculations of of (**a**) *n*, (**b**) N_M, (**c**) Q_{sat}, and (**d**) ΔE as a condition of temperature for MB adsorption.

Table S2 in the Supplementary Materials presents the *n* values related to the MB uptake as the temperature increased, providing the values of 1.97 (25 °C), 1.87 (40 °C), and 1.14 (55 °C). So, the third condition was achieved during the MB-ANZ/TC/MNPs interaction based on the three previously stated conditions. Consequently, the eliminated MB molecules were arranged vertically, and at every solution temperature, a functional group of the fabricated magnetic biosorbent can capture numerous MB molecules (i.e., multi-interaction mechanism). The low level of MB aggregation at 55 °C suggested that

this dye could be quickly removed from the ANZ/TC/MNPs surface at different functional groups of this adsorbent prior to its aggregation in solution. Furthermore, the MB-MB aggregation in solutions (i.e., before adsorption) was predictable. Moreover, it is evident that the temperature increase had no effect on the adsorbate's geometry or the adsorption mechanism.

3.5.2. The N_M Parameter

Figure 9 displays the performance of the N_M parameter for MB removal by the ANZ/TC/MNPs composite at 25°, 40°, and 55 °C. The N_M value improved from 27.7 to 142.17 mg/g within 25° to 55 °C (see Table S2). The removal of MB molecules may have been aided by the addition of new active sites, which became more efficient at higher temperatures, as evidenced by the parameter's increase with an increase in temperature. Additionally, the endothermic type of the adsorption process was supported by raising this steric factor as temperature increased. Raising the solution temperature to 55 °C clearly decreased the MB aggregation and regularly enabled more dye molecules to hold added ANZ/TC/MNPs receptor sites. Overall, when the solution temperature is changed, the tendencies for the n and N_M parameters usually show opposite outlines [9,34,47].

3.5.3. The Q_{sat} Parameter

The adsorption ability of the ANZ/TC/MNPs composite in removing MB molecules is assessed via determination of this steric parameter [21]. The Q_{sat} was 109.16, 159.4, and 324.14 mg/g at 25, 40, and 55 °C, respectively (Table S2 and Figure 9). The endothermic behavior between the MB dye and the ANZ/TC/MNPs effective sites was confirmed by increasing the Q_{sat} with raising the uptake temperature. It is noticeable that as the temperature increased, the Q_{sat} and N_M factors showed the same affinity (see Figure 9). In general, the adsorbate's mobility and kinetics improved in the solution with rising temperature, leading to an increase in the number of interactions between the MB molecules and the newly occupied ANZ/TC/MNPs active sites. This behavior contributed significantly to the rise in the N_M parameter and frequently, the corresponding Q_{sat} one at each temperature. Consequently, the main variable influencing the ANZ/TC/MNPs adsorption capacity was the steric N_M parameter.

3.5.4. Energetic Parameters (ΔE)

The values of the MB adsorption energies in relation to each solution temperatures are shown in Figure 9. At all temperatures, the ΔE_1 and ΔE_2 were positive, indicating an endothermic interaction between MB and ANZ/TC/MNPs. As expected, at all temperatures, the ΔE_1 values were greater than the ΔE_2 values (i.e., MB–MB interface was lower than the MB–adsorbent interaction). Also, the obtained energies were less than 25 kJ/mol, indicating that MB molecules and the active sites of ANZ/TC/MNPs were subject to physical interactions like electrostatic and hydrogen bonds. During the adsorption process, hydrogen bonding between the -OH groups of the ANZ/TC/MNPs surface and the aromatic rings of the MB structure is possible. Additionally, a major element of the removal system was the electrostatic attraction between the cationic MB molecules and the tested adsorbent's negative active sites. Additionally, the produced magnetic biosorbent displayed a mesoporous structure, which suggested that filling of the adsorbent pores may be involved during the adsorption system. It can be observed that as temperature increased, both the steric Q_{sat} and the energetic ΔE values improved. Based on our knowledge of steric and energetic characteristics, we can therefore conclude that the steric (N_M) and energetic (ΔE) parameters were the main factors affecting the MB adsorption performance and mechanism on ANZ/TC/MNPs. Figure 10 illustrates the prospective mechanism of interaction between the functional groups of ANZ/TC/MNPs and MB molecules, as set up by the experiments and the physicochemical parameters of the double-layer model.
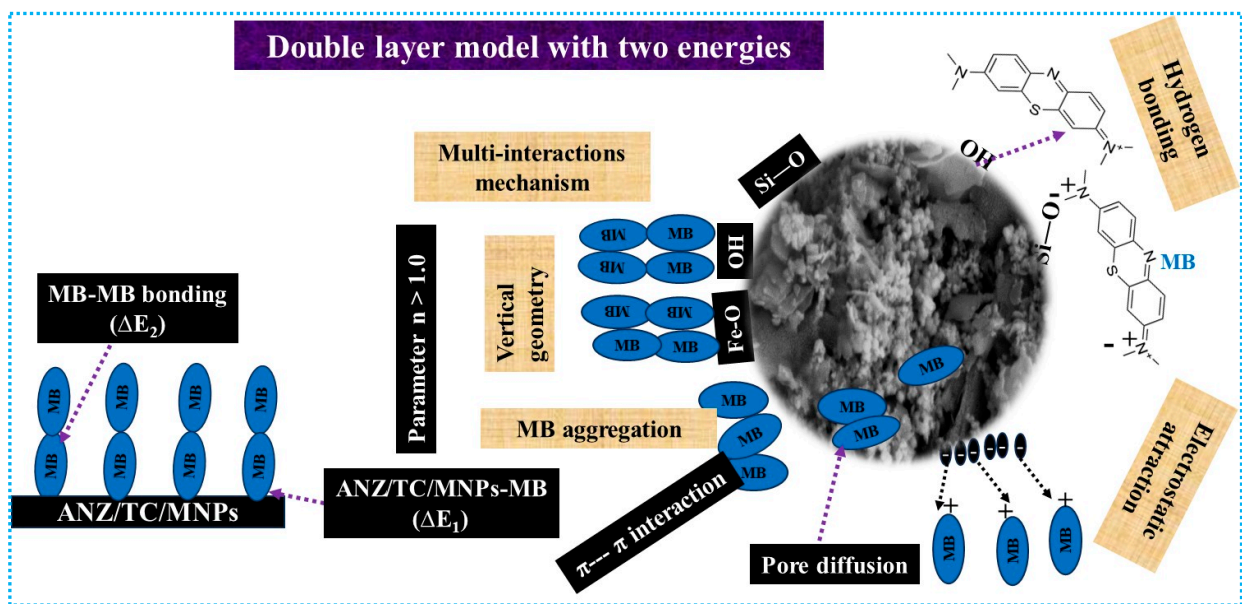
Figure 10. The probable interaction mechanisms between MB dye and ANZ/TC/MNPs adsorbent.

3.6. Thermodynamic Functions

3.6.1. Entropy

Figure 11a shows how the entropy factor changes with MB concentration at various temperatures. Prior to the half-saturation concentration, the MB adsorption system's disorder degree increased as the MB concentration increased until it reached its maximum value. The active adsorption sites of ANZ/TC/MNPs are typically empty at the start of the MB uptake process, which allows the MB molecules to interact with a great number of effective sites. In the context of an order case, a decrease in the entropy parameter was noted as a result of MB molecules filling ANZ/TC/MNPs, particularly after half-saturation. Finally, the achievement of zero entropy signifies the complete saturation of every active site in ANZ/TC/MNPs [20].
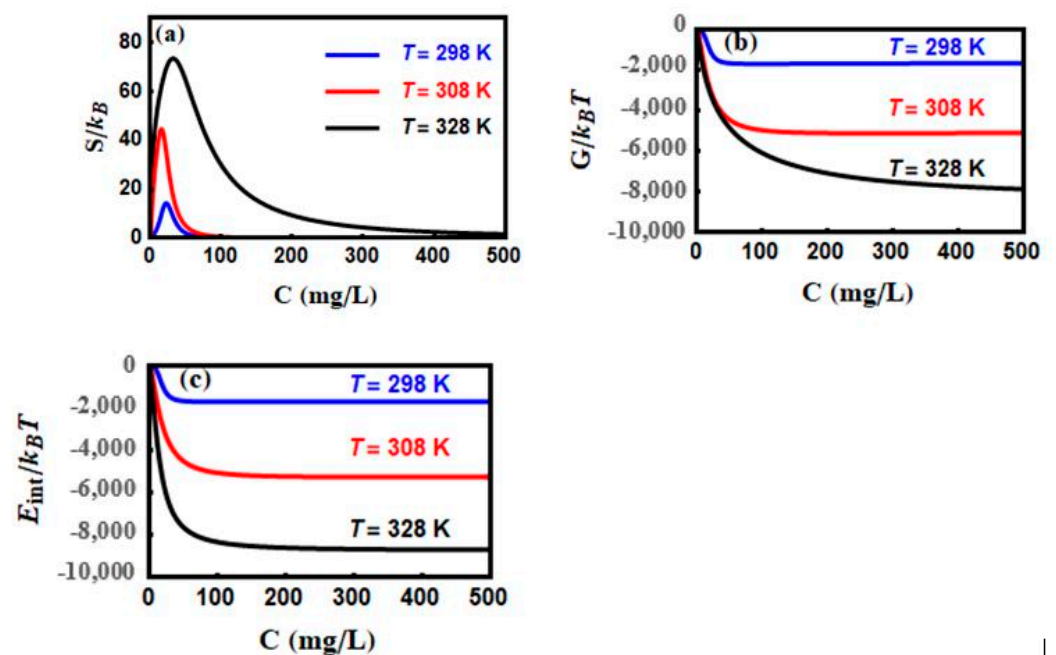

Figure 11. Assessment of thermodynamic functions entropy (**a**), Gibbs free energy (**b**), and internal energy (**c**) at temperatures of 25, 40, and 55 °C.

3.6.2. Gibbs Free Energy

Figure 11b displays the conduct of this thermodynamic parameter with the dye concentrations. At all temperatures, the Gibbs free energy was negative, which led to us suppose that the MB adsorption system was thermodynamically spontaneous [21]. Additionally, at very low dye concentrations, the Gibbs free energy began at zero and frequently decreased as the adsorbate concentration increased.

3.6.3. Internal Energy

The behavior of internal energy varied as the MB concentration increased, as seen in Figure 11c. The adsorption system's ability to release energy to the outside was designated by the negative value of internal energy, which suggested a high level of interaction between the MB molecules and the ANZ/TC/MNPs product [20,21]. Furthermore, the interface between the MB and the ANZ/TC/MNPs happened spontaneously according to the internal energy values that were negative.

3.7. Salinity Effect on MB Adsorption

When the concentration of salt was raised from 0.2 to 1.2 g/L, it was observed that the removed amounts of the tested MB dye decreased from 86 to 71 mg/g (Figure 12). This could be a result of salt ions' screening action, which resulted in inhibiting the MB-ANZ/TC/MNPs electrostatic attractions [12]. Furthermore, this decrease in the MB uptake values might be related to the occupation of specific ANZ/TC/MNPs active sites by sodium ions.
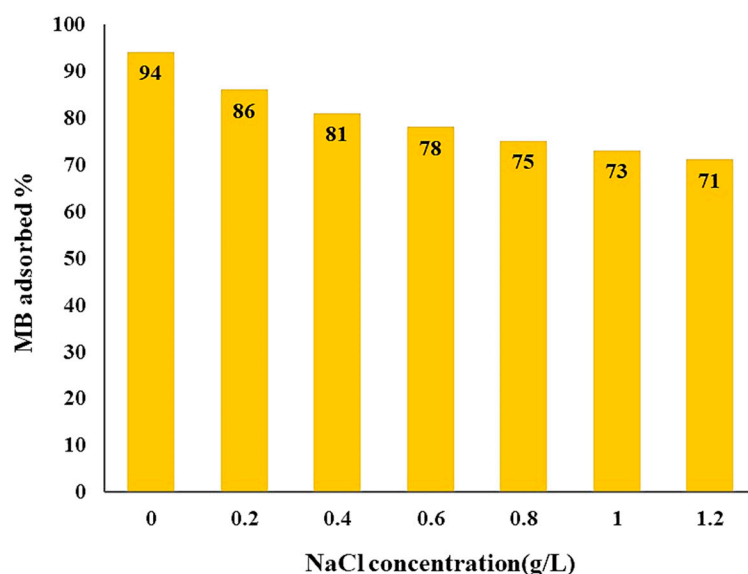

Figure 12. Effect of NaCl concentration on the removed amount of MB dye.

3.8. Reusability and Stability of ANZ/TC/MNPs Adsorbent

The outcomes of five consecutive regeneration and repurposing cycles of the prepared magnetic ANZ/TC/MNPs adsorbent for the removal of MB were considered. The percentages of 93, 87, 83, 78, and 74% of MB uptake were achieved after the first, second, third, fourth, and the last cycles (see Figure 13). According to this result, the magnetic adsorbent can efficiently remove MB several times without suffering a major reduction in its adsorption effectiveness. In summary, ANZ/TC/MNPs is a helpful adsorbent and can be used in industrial applications.
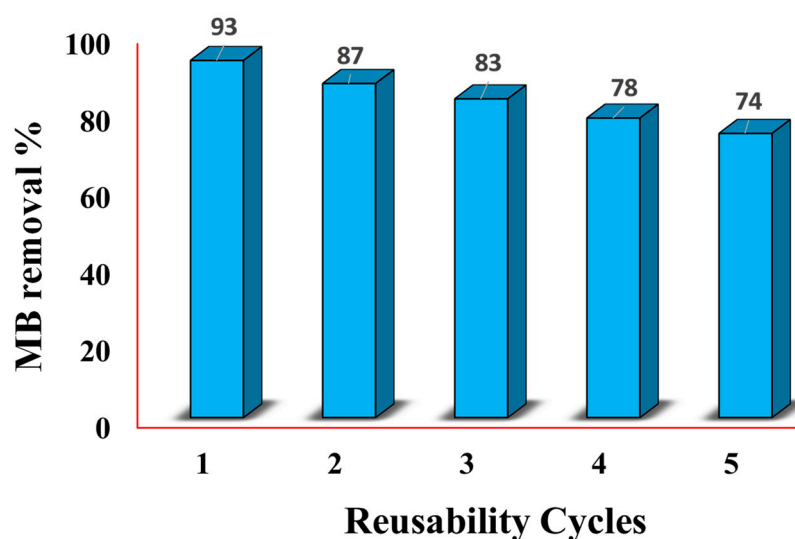
Figure 13. Reusability evaluation of ANZ/TC/MNPs for MB after five regeneration cycles.

3.9. Comparison with Other Adsorbents

The maximum MB adsorption capacity by ANZ/TC/MNPs in comparison to multiple raw (e.g., montmorillonite and zeolite) and modified (e.g., magnetic serpentine, Fe_2O_3/montmorillonite, and SDBS-modified zeolite) materials is listed in Table 2. Consequently, the as-synthesized ANZ/TC/MNPs is recommended as a promising magnetic biosorbent for the remediation of water contaminated with MB dye.

Table 2. Comparison of sorption capacities for dissimilar materials and the developed ANZ/TC/MNPs.

Adsorbent	q_{max} (mg/g)	References
PVA/CMC/TUR film	102	[28]
Montmorillonite (Mt)	64.43	[31]
Fe_2O_3-Mt	106.38	[31]
OMWCNT-Fe_2O_3	1.11	[32]
OMWCNT-κ-carrageenan-Fe_3O_4	1.24	[32]
Magnetic montmorillonite	69	[49]
Zeolite	8.67	[50]
SDBS-modified zeolite	15.68	[50]
Fibrous clay minerals	39–85	[51]
Fe_3O_4/serpentine composite	201	[12]
Treated ball clay	25	[52]
ANZ/TC/MNPs	268.67	Current study

4. Conclusions

A biodegradable and eco-friendly magnetic nanocomposite (ANZ/TC/MNPs) based on combining the H_2O_2-activated zeolite/turmeric carbohydrate polymer combination with magnetite nanoparticles was successfully synthesized, characterized, and used in MB adsorption. MB adsorption was carried out at pH 8.0 solution, dye concentration (25–200 mg/L), shaking time (2 h), and a temperature range of 25–55 °C. Equilibrium models following the assumptions of conventional and statistical physics theories were applied. The MB adsorption results were fitted by both the conventional Freundlich model and the statistical double-layer adsorption model. With values ranging from 268.67 to 307.73 mg/g, the tested composite's maximum uptake capacities were greater than those of other adsorbents. A vertical geometry and multiple interactions mechanism were proposed by the steric parameters. Energetically, physical forces such as electrostatic

interactions and hydrogen bonds were outlined. Thermodynamic analysis revealed the endothermic and spontaneous nature of the MB adsorption system. The high stability of the magnetic biosorbent and its prospective industrial applications were confirmed by the characterization, adsorption, and regeneration results.

Supplementary Materials: The following supporting information can be downloaded at: https://www.mdpi.com/article/10.3390/magnetochemistry10110091/s1.

References

1. Sheikh, M.C.; Hasan, M.M.; Hasan, M.N.; Salman, M.S.; Kubra, K.T.; Awual, M.E.; Waliullah, R.; Rasee, A.I.; Rehan, A.I.; Hossain, M.S. Toxic cadmium (II) monitoring and removal from aqueous solution using ligand-based facial composite adsorbent. *J. Mol. Liq.* **2023**, *389*, 122854. [CrossRef]
2. Rasee, A.I.; Awual, E.; Rehan, A.I.; Hossain, M.S.; Waliullah, R.; Kubra, K.T.; Sheikh, M.C.; Salman, M.S.; Hasan, M.N.; Hasan, M.M. Efficient separation, adsorption, and recovery of Samarium (III) ions using novel ligand-based composite adsorbent. *Surf. Interfaces* **2023**, *41*, 103276. [CrossRef]
3. Waliullah, R.; Rehan, A.I.; Awual, M.E.; Rasee, A.I.; Sheikh, M.C.; Salman, M.S.; Hossain, M.S.; Hasan, M.M.; Kubra, K.T.; Hasan, M.N. Optimization of toxic dye removal from contaminated water using chitosan-grafted novel nanocomposite adsorbent. *J. Mol. Liq.* **2023**, *388*, 122763. [CrossRef]
4. Rehan, A.I.; Rasee, A.I.; Awual, M.E.; Waliullah, R.; Hossain, M.S.; Kubra, K.T.; Salman, M.S.; Hasan, M.M.; Hasan, M.N.; Sheikh, M.C. Improving toxic dye removal and remediation using novel nanocomposite fibrous adsorbent. *Colloids Surf. A Physicochem. Eng. Asp.* **2023**, *673*, 131859. [CrossRef]
5. Awual, M.R.; Hasan, M.N.; Hasan, M.M.; Salman, M.S.; Sheikh, M.C.; Kubra, K.T.; Islam, M.S.; Marwani, H.M.; Islam, A.; Khaleque, M.A. Green and robust adsorption and recovery of Europium (III) with a mechanism using hybrid donor conjugate materials. *Sep. Purif. Technol.* **2023**, *319*, 124088. [CrossRef]
6. Hasan, M.M.; Salman, M.S.; Hasan, M.N.; Rehan, A.I.; Awual, M.E.; Rasee, A.I.; Waliullah, R.; Hossain, M.S.; Kubra, K.T.; Sheikh, M.C. Facial conjugate adsorbent for sustainable Pb (II) ion monitoring and removal from contaminated water. *Colloids Surf. A Physicochem. Eng. Asp.* **2023**, *673*, 131794. [CrossRef]
7. Awual, M.R. Novel conjugated hybrid material for efficient lead (II) capturing from contaminated wastewater. *Mater. Sci. Eng. C* **2019**, *101*, 686–695. [CrossRef]
8. Hasan, M.N.; Shenashen, M.; Hasan, M.M.; Znad, H.; Awual, M.R. Assessing of cesium removal from wastewater using functionalized wood cellulosic adsorbent. *Chemosphere* **2021**, *270*, 128668. [CrossRef]
9. Shakly, M.; Saad, L.; Seliem, M.K.; Bonilla-Petriciolet, A.; Shehata, N. New insights into the selective adsorption mechanism of cationic and anionic dyes using MIL-101 (Fe) metal-organic framework: Modeling and interpretation of physicochemical parameters. *J. Contam. Hydrol.* **2022**, *247*, 103977. [CrossRef]
10. Barakat, M.A.; Selim, A.Q.; Mobarak, M.; Kumar, R.; Anastopoulos, I.; Giannakoudakis, D.; Bonilla-Petriciolet, A.; Mohamed, E.A.; Seliem, M.K.; Komarneni, S. Experimental and theoretical studies of methyl orange uptake by Mn–rich synthetic mica: Insights into manganese role in adsorption and selectivity. *Nanomaterials* **2020**, *10*, 1464. [CrossRef]

11. Barakat, M.; Kumar, R.; Lima, E.C.; Seliem, M.K. Facile synthesis of muscovite–supported Fe$_3$O$_4$ nanoparticles as an adsorbent and heterogeneous catalyst for effective removal of methyl orange: Characterisation, modelling, and mechanism. *J. Taiwan Inst. Chem. Eng.* **2021**, *119*, 146–157. [CrossRef]

12. Seliem, M.K.; Barczak, M.; Anastopoulos, I.; Giannakoudakis, D.A. A novel nanocomposite of activated serpentine mineral decorated with magnetic nanoparticles for rapid and effective adsorption of hazardous cationic dyes: Kinetics and equilibrium studies. *Nanomaterials* **2020**, *10*, 684. [CrossRef] [PubMed]

13. Kubra, K.T.; Salman, M.S.; Hasan, M.N. Enhanced toxic dye removal from wastewater using biodegradable polymeric natural adsorbent. *J. Mol. Liq.* **2021**, *328*, 115468. [CrossRef]

14. Yeamin, M.B.; Islam, M.M.; Chowdhury, A.-N.; Awual, M.R. Efficient encapsulation of toxic dyes from wastewater using several biodegradable natural polymers and their composites. *J. Clean. Prod.* **2021**, *291*, 125920. [CrossRef]

15. Mobarak, M.; Selim, A.Q.; Mohamed, E.A.; Seliem, M.K. A superior adsorbent of CTAB/H$_2$O$_2$ solution−modified organic carbon rich-clay for hexavalent chromium and methyl orange uptake from solutions. *J. Mol. Liq.* **2018**, *259*, 384–397. [CrossRef]

16. Mobarak, M.; Ali, R.A.; Seliem, M.K. Chitosan/activated coal composite as an effective adsorbent for Mn (VII): Modeling and interpretation of physicochemical parameters. *Int. J. Biol. Macromol.* **2021**, *186*, 750–758. [CrossRef]

17. Kamel, R.M.; Shahat, A.; Hegazy, W.H.; Khodier, E.M.; Awual, M.R. Efficient toxic nitrite monitoring and removal from aqueous media with ligand based conjugate materials. *J. Mol. Liq.* **2019**, *285*, 20–26. [CrossRef]

18. Mohamed, E.A.; Selim, A.Q.; Ahmed, S.A.; Sellaoui, L.; Bonilla-Petriciolet, A.; Erto, A.; Li, Z.; Li, Y.; Seliem, M.K. H$_2$O$_2$-activated anthracite impregnated with chitosan as a novel composite for Cr (VI) and methyl orange adsorption in single-compound and binary systems: Modeling and mechanism interpretation. *Chem. Eng. J.* **2020**, *380*, 122445. [CrossRef]

19. Awual, M.R.; Yaita, T.; Kobayashi, T.; Shiwaku, H.; Suzuki, S. Improving cesium removal to clean-up the contaminated water using modified conjugate material. *J. Environ. Chem. Eng.* **2020**, *8*, 103684. [CrossRef]

20. Mobarak, M.; Qaysi, S.; Ahmed, M.S.; Salama, Y.F.; Abbass, A.M.; Abd Elrahman, M.; Abdel-Gawwad, H.A.; Seliem, M.K. Insights into the adsorption performance and mechanism of Cr (VI) onto porous nanocomposite prepared from gossans and modified coal interface: Steric, energetic, and thermodynamic parameters interpretations. *Chin. J. Chem. Eng.* **2023**, *61*, 118–128. [CrossRef]

21. Badawy, A.M.; Farghali, A.A.; Bonilla-Petriciolet, A.; Seliem, M.K.; Selim, A.Q.; Ali, M.A.; Al-Dossari, M.; Abd EL-Gawaad, N.; Mobarak, M.; Lima, E.C. Facile synthesis of a recyclable multifunctional magnetic adsorbent prepared from H$_2$O$_2$-modified carbon clay/rice flour polymer/Fe$_3$O$_4$ nanoparticles interface for effective removal of ibuprofen. *J. Taiwan Inst. Chem. Eng.* **2023**, *152*, 105177. [CrossRef]

22. Seliem, M.K.; Komarneni, S. Equilibrium and kinetic studies for adsorption of iron from aqueous solution by synthetic Na-A zeolites: Statistical modeling and optimization. *Microporous Mesoporous Mater.* **2016**, *228*, 266–274. [CrossRef]

23. Abukhadra, M.; Mohamed, A. Adsorption removal of safranin dye contaminants from water using various types of natural zeolite. *Silicon* **2019**, *11*, 1635–1647. [CrossRef]

24. Ferri, B.B.; Wernke, G.; Resende, J.F.; Ribeiro, A.C.; Cusioli, L.F.; Bergamasco, R.; Vieira, M.F. Natural zeolite as adsorbent for metformin removal from aqueous solutions: Adsorption and regeneration properties. *Desalination Water Treat.* **2024**, *320*, 100602. [CrossRef]

25. Abukhadra, M.R.; Mostafa, M.; Jumah, M.N.B.; Al-Khalawi, N.; Alruhaimi, R.S.; Salama, Y.F.; Allam, A.A. Insight into the adsorption properties of chitosan/zeolite-A hybrid structure for effective decontamination of toxic Cd (II) and As (V) ions from the aqueous environments. *J. Polym. Environ.* **2022**, *30*, 295–307. [CrossRef]

26. Mohseni-Bandpi, A.; Al-Musawi, T.J.; Ghahramani, E.; Zarrabi, M.; Mohebi, S.; Vahed, S.A. Improvement of zeolite adsorption capacity for cephalexin by coating with magnetic Fe$_3$O$_4$ nanoparticles. *J. Mol. Liq.* **2016**, *218*, 615–624. [CrossRef]

27. Neolaka, Y.A.; Lawa, Y.; Naat, J.; Riwu, A.A.; Mango, A.W.; Darmokoesoemo, H.; Widyaningrum, B.A.; Iqbal, M.; Kusuma, H.S. Efficiency of activated natural zeolite-based magnetic composite (ANZ-Fe$_3$O$_4$) as a novel adsorbent for removal of Cr (VI) from wastewater. *J. Mater. Res. Technol.* **2022**, *18*, 2896–2909. [CrossRef]

28. Radoor, S.; Karayil, J.; Jayakumar, A.; Parameswaranpillai, J.; Lee, J.; Siengchin, S. Ecofriendly and low-cost bio adsorbent for efficient removal of methylene blue from aqueous solution. *Sci. Rep.* **2022**, *12*, 20580. [CrossRef]

29. Keyhanian, F.; Shariati, S.; Faraji, M.; Hesabi, M. Magnetite nanoparticles with surface modification for removal of methyl violet from aqueous solutions. *Arab. J. Chem.* **2016**, *9*, S348–S354. [CrossRef]

30. Ebrahimian Pirbazari, A.; Saberikhah, E.; Gholami Ahmad Gorabi, N. Fe$_3$O$_4$ nanoparticles loaded onto wheat straw: An efficient adsorbent for Basic Blue 9 adsorption from aqueous solution. *Desalination Water Treat.* **2016**, *57*, 4110–4121. [CrossRef]

31. Chang, J.; Ma, J.; Ma, Q.; Zhang, D.; Qiao, N.; Hu, M.; Ma, H. Adsorption of methylene blue onto Fe3O4/activated montmorillonite nanocomposite. *Appl. Clay Sci.* **2016**, *119*, 132–140. [CrossRef]

32. Duman, O.; Tunç, S.; Polat, T.G.; Bozoğlan, B.K. Synthesis of magnetic oxidized multiwalled carbon nanotube-κ-carrageenan-Fe$_3$O$_4$ nanocomposite adsorbent and its application in cationic Methylene Blue dye adsorption. *Carbohydr. Polym.* **2016**, *147*, 79–88. [CrossRef] [PubMed]

33. Duman, O.; Özcan, C.; Polat, T.G.; Tunç, S. Carbon nanotube-based magnetic and non-magnetic adsorbents for the high-efficiency removal of diquat dibromide herbicide from water: OMWCNT, OMWCNT-Fe$_3$O$_4$ and OMWCNT-κ-carrageenan-Fe$_3$O$_4$ nanocomposites. *Environ. Pollut.* **2019**, *244*, 723–732. [CrossRef] [PubMed]

34. Abu Sharib, A.S.A.; Bonilla-Petriciolet, A.; Selim, A.Q.; Mohamed, E.A.; Seliem, M.K. Utilizing modified weathered basalt as a novel approach in the preparation of Fe3O4 nanoparticles: Experimental and theoretical studies for crystal violet adsorption. *J. Environ. Chem. Eng.* **2021**, *9*, 106220. [CrossRef]

35. Brunauer, S.; Emmett, P.H.; Teller, E. Adsorption of gases in multimolecular layers. *J. Am. Chem. Soc.* **1938**, *60*, 309–319. [CrossRef]

36. Langmuir, I. The constitution and fundamental properties of solids and liquids. Part I. Solids. *J. Am. Chem. Soc.* **1916**, *38*, 2221–2295. [CrossRef]

37. Freundlich, H. Over the Adsorption in Solution. *J. Phys. Chem. A* **1906**, *57*, 385–470.

38. Yosefi, L.; Haghighi, M.; Allahyari, S.; Ashkriz, S. Effect of ultrasound irradiation and Ni-loading on properties and performance of CeO$_2$-doped Ni/clinoptilolite nanocatalyst used in polluted air treatment. *Process Saf. Environ. Prot.* **2015**, *95*, 26–37. [CrossRef]

39. Cocean, I.; Cocean, A.; Postolachi, C.; Pohoata, V.; Cimpoesu, N.; Bulai, G.; Iacomi, F.; Gurlui, S. Alpha keratin amino acids BEHVIOR under high FLUENCE laser interaction. Medical applications. *Appl. Surf. Sci.* **2019**, *488*, 418–426. [CrossRef]

40. Li, L.; Tian, F.; Qiu, L.; Wu, F.; Yang, W.; Yu, Y. Recent Progress on Ruthenium-Based Electrocatalysts towards the Hydrogen Evolution Reaction. *Catalysts* **2023**, *13*, 1497. [CrossRef]

41. Li, L.; Tian, F.; Wu, F.; Qiu, L.; Geng, S.; Li, M.; Chen, Z.; Yang, W.; Liu, Y.; Yu, Y. Strong electronic metal-support interaction of Ni4Mo/N-SrMoO4 promotes alkaline hydrogen electrocatalysis. *Appl. Catal. B Environ. Energy* **2025**, *361*, 124660. [CrossRef]

42. Nayl, A.A.; Abd-Elhamid, A.I.; Ahmed, I.M.; Bräse, S. Preparation and characterization of magnetite talc (Fe$_3$O$_4$@ Talc) nanocomposite as an effective adsorbent for Cr (VI) and alizarin red S dye. *Materials* **2022**, *15*, 3401. [CrossRef] [PubMed]

43. Petrinic, I.; Stergar, J.; Bukšek, H.; Drofenik, M.; Gyergyek, S.; Hélix-Nielsen, C.; Ban, I. Superparamagnetic Fe$_3$O$_4$@ CA nanoparticles and their potential as draw solution agents in forward osmosis. *Nanomaterials* **2021**, *11*, 2965. [CrossRef]

44. Thommes, M.; Kaneko, K.; Neimark, A.V.; Olivier, J.P.; Rodriguez-Reinoso, F.; Rouquerol, J.; Sing, K.S. Physisorption of gases, with special reference to the evaluation of surface area and pore size distribution (IUPAC Technical Report). *Pure Appl. Chem.* **2015**, *87*, 1051–1069. [CrossRef]

45. Wu, J.; Yang, J.; Huang, G.; Xu, C.; Lin, B. Hydrothermal carbonization synthesis of cassava slag biochar with excellent adsorption performance for Rhodamine B. *J. Clean. Prod.* **2020**, *251*, 119717. [CrossRef]

46. Horie, M.; Fujita, K. Toxicity of metal oxides nanoparticles. In *Advances in Molecular Toxicology*; Elsevier: Amsterdam, The Netherlands, 2011; Volume 5, pp. 145–178.

47. Ramadan, H.; Mobarak, M.; Lima, E.C.; Bonilla-Petriciolet, A.; Li, Z.; Seliem, M.K. Cr (VI) adsorption onto a new composite prepared from Meidum black clay and pomegranate peel extract: Experiments and physicochemical interpretations. *J. Environ. Chem. Eng.* **2021**, *9*, 105352. [CrossRef]

48. Li, Z.; Sellaoui, L.; Dotto, G.L.; Lamine, A.B.; Bonilla-Petriciolet, A.; Hanafy, H.; Belmabrouk, H.; Netto, M.S.; Erto, A. Interpretation of the adsorption mechanism of Reactive Black 5 and Ponceau 4R dyes on chitosan/polyamide nanofibers via advanced statistical physics model. *J. Mol. Liq.* **2019**, *285*, 165–170. [CrossRef]

49. Cottet, L.; Almeida, C.; Naidek, N.; Viante, M.; Lopes, M.; Debacher, N. Adsorption characteristics of montmorillonite clay modified with iron oxide with respect to methylene blue in aqueous media. *Appl. Clay Sci.* **2014**, *95*, 25–31. [CrossRef]

50. Rida, K.; Bouraoui, S.; Hadnine, S. Adsorption of methylene blue from aqueous solution by kaolin and zeolite. *Appl. Clay Sci.* **2013**, *83*, 99–105. [CrossRef]

51. Hajjaji, M.; Alami, A.; El Bouadili, A. Removal of methylene blue from aqueous solution by fibrous clay minerals. *J. Hazard. Mater.* **2006**, *135*, 188–192. [CrossRef]

52. Auta, M.; Hameed, B. Modified mesoporous clay adsorbent for adsorption isotherm and kinetics of methylene blue. *Chem. Eng. J.* **2012**, *198*, 219–227. [CrossRef]